

Ultrahigh-Resolution, Label-Free Hyperlens Imaging in the Mid-IR

Mingze He,[○] Ganjigunte R. S. Iyer,[○] Shaurya Aarav,[○] Sai S. Sunku, Alexander J. Giles, Thomas G. Folland, Nicholas Sharac, Xiaohang Sun, Joseph Matson, Song Liu, James H. Edgar, Jason W. Fleischer, D. N. Basov, and Joshua D. Caldwell*

 Cite This: *Nano Lett.* 2021, 21, 7921–7928

 Read Online

ACCESS |

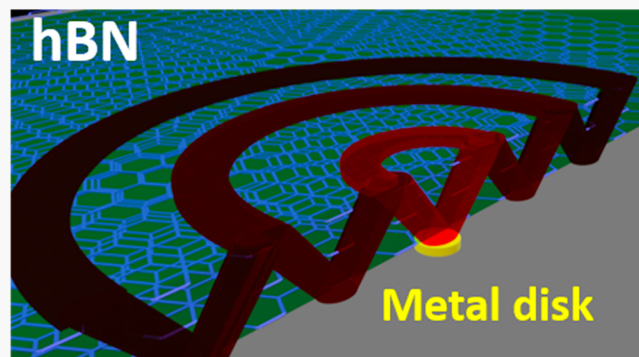
 Metrics & More

 Article Recommendations

 Supporting Information

ABSTRACT: The hyperbolic phonon polaritons supported in hexagonal boron nitride (hBN) with long scattering lifetimes are advantageous for applications such as super-resolution imaging via hyperlensing. Yet, hyperlens imaging is challenging for distinguishing individual and closely spaced objects and for correlating the complicated hyperlens fields with the structure of an unknown object underneath. Here, we make significant strides to overcome each of these challenges. First, we demonstrate that monoisotopic $h^{11}\text{BN}$ provides significant improvements in spatial resolution, experimentally resolving structures as small as 44 nm and those with sub 25 nm spacings at $6.76\ \mu\text{m}$ free-space wavelength. We also present an image reconstruction algorithm that provides a structurally accurate, visual representation of the embedded objects from the complex hyperlens field. Further, we offer additional insights into optimizing hyperlens performance on the basis of material properties, with an eye toward realizing far-field imaging modalities. Thus, our results significantly advance label-free, high-resolution, spectrally selective hyperlens imaging and image reconstruction methodologies.

KEYWORDS: *hyperlens, hyperbolic media, reconstruction algorithm, super-resolution*



Subdiffractive imaging in conventional optical microscopy is not possible due to Abbe's diffraction limit, as light containing the high momentum information necessary for imaging deeply subwavelength objects is evanescent and thus rapidly decays from the surface and does not propagate into the far field. The hyperlens concept provides a promising approach to overcome this challenge. This approach exploits hyperbolic polaritons (HPs) supported in highly anisotropic materials exhibiting a dielectric permittivity tensor that is opposite in sign along orthogonal directions, e.g., $(\epsilon_t > 0, \epsilon_z < 0)$ or $(\epsilon_t < 0, \epsilon_z > 0)$, where $\epsilon_t = \epsilon_x = \epsilon_y$ and ϵ_z are tangential and axial permittivities, respectively.^{1–3} In this hyperbolic spectral region, high- k wavevectors can propagate at an angle θ dictated by the material dispersion, with θ defined to the surface normal (z axis)^{4–8} as follows:

$$\theta = \pi/2 - \arctan(\sqrt{\epsilon_z}/i\sqrt{\epsilon_t}) \quad (1)$$

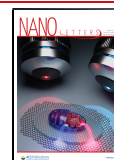
The scattering of light off of a subdiffractive object can therefore launch HPs into the hyperbolic slab, which will then propagate at this frequency-dependent angle to the opposite surface (Figure 1a). For a curved hyperbolic material,^{6,9–12} these hyperbolic “rays” propagating along the radial directions are expanded, resulting in magnified hyperlens fields resolvable in the far field. Far-field hyperlenses are also possible through metalens designs integrated with planar hyperbolic materi-

als.^{13,14} In addition to measurements in the far field, the hyperlens performance can be evaluated in the near field via probes such as scattering-type scanning near-field optical microscopy (s-SNOM),^{5,8} which we have employed here. Besides hyperlens imaging, the same concept has been exploited to enhance light–matter interactions^{8,15} and lithography with demagnifying.⁷

Hyperlensing for sub-diffraction-limited imaging was initially demonstrated with artificial hyperbolic metamaterials (HMMs):⁹ i.e., metal and dielectric stacks.^{9,10} However, these HMMs suffer from inherently high optical losses from metallic layers, limiting the transmission efficiency and spatial resolution.¹¹ In contrast, natural hyperbolic materials,^{5,8,16–18} such as hexagonal boron nitride (hBN), support low-loss hyperbolic phonon polaritons (HPhPs) suitable for hyperlens imaging.^{5,8,16} Still, the spatial resolution and the HPhP transmission of hBN-enabled hyperlenses remain restricted by loss. Further, instead of magnified images, the collected

Received: May 8, 2021

Published: September 17, 2021



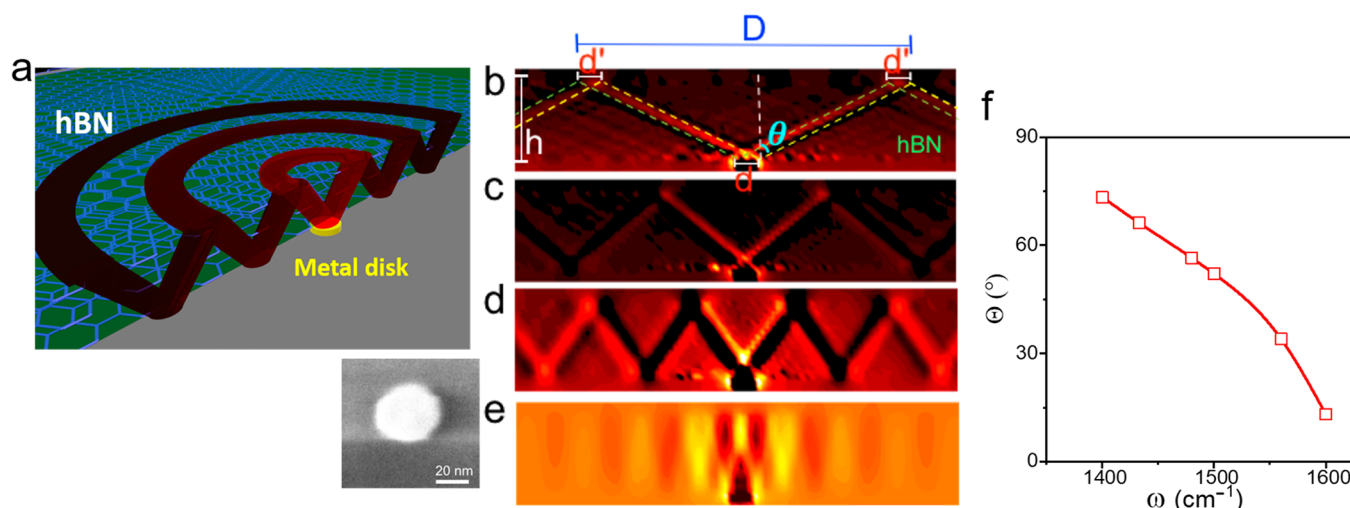


Figure 1. Subdiffractive focusing and imaging through hBN. (a) Schematic illustration of the hot rings/fringes on the top surface and within the hBN as a result of multiple reflections of the HPhPs launched from the edges of the subdiffractive nickel disks embedded beneath a 125 nm thick h¹¹BN slab. Inset: an SEM image of the 44 nm disk. (b–e) Simulated cross-sectional *E*-field distributions for a 40 nm disk embedded under a 125 nm thick h¹¹BN flake at $\omega = 1433, 1500, 1560,$ and 1600 cm^{-1} , respectively. (f) Calculated propagation angle (θ) of HPhPs within h¹¹BN as a function of frequency. Open squares represent the frequencies where simulations and experiments were performed.

hyperlens fields represent complex products of (subwavelength) diffraction, posing challenges in identification of the imaged objects. Notably, both far-field and near-field hyperlenses are restricted by those factors.

Here we address these challenges by combining material developments with an image reconstruction algorithm. By the implementation of monoisotopic h¹¹BN (>99%), optical loss is reduced 3-fold in comparison with naturally abundant (NA) hBN, which allows us to resolve objects with a diameter as small as 44 nm and interparticle gaps (pitch) of <25 nm (125 nm), representing normalized resolutions of λ_{FS} (free space wavelength, $6.76 \mu\text{m}$) over 154 and 270 (54), respectively. Furthermore, the peak signal to noise ratio (PSNR) of hyperlens fields from monoisotopic hBN is also increased 3-fold, potentially allowing smaller features to be imaged. Moreover, we provide a back-propagation method to identify spatial locations and sizes of unknown objects from the hyperlens fields, potentially enabling on-the-fly conversion of the collected hyperlens fields into object images. In addition, we also offer insights into optimizing hyperlens performance from a material perspective. Therefore, the combination of monoisotopic h¹¹BN and computational image processing provides significant advancements toward practical mid-infrared (MIR) hyperlens designs and lays the foundation for functional spectroscopic hyperlens imaging.

Frequency-dependent hyperlensing can be described via a ray-tracing picture (Figure 1a). Here, evanescent fields are produced as long-wavelength MIR light is scattered by a subdiffractive object, which launches propagating HPhPs due to the requisite momentum and the proximity to the hyperbolic slab. These volume-confined HPhPs propagate at the frequency-dependent angle through the slab, carrying the high spatial information (eq 1) to the opposite surface of the hBN,¹ where they are reflected and create an evanescent field above the top surface of the hBN (Figure 1). With metasurface designs placed onto a flat hyperbolic material and/or curving a thick slab of a hyperbolic material,^{9–14} these HPhP modes can propagate into the far field to enable direct imaging of subdiffractive objects. Here, we simplify the evaluation of

hyperlens performance and our image reconstruction algorithm by probing the near-field response by s-SNOM,^{5,8} so that no modifications of the hyperbolic media topography are required. Importantly, the reported advancements here are equally applicable to either a metalens or a curved hyperlens approach.

To experimentally demonstrate the benefits of our monoisotopic hBN enabled hyperlens, we fabricated a series of nickel structures by electron beam lithography and a standard lift-off procedure (see Methods), after which flakes of NA (~125 nm thick) and ¹¹B-enriched (>99%) hBN (~125 nm thick) were mechanically exfoliated and transferred on top of these nickel disks. While both ¹⁰B- and ¹¹B-enriched hBN have been grown in high purity^{19–21} with enhanced phonon lifetimes over NA materials,^{22,23} h¹¹BN (>99%¹¹B) was employed due to the near-negligible spectral shift in the optic phonons, i.e., $\omega_{\text{TO}} \approx 1359.8 \text{ cm}^{-1}$ and $\omega_{\text{LO}} \approx 1608.7 \text{ cm}^{-1}$ with respect to NA material ($\omega_{\text{TO}} \approx 1360 \text{ cm}^{-1}$ and $\omega_{\text{LO}} \approx 1614 \text{ cm}^{-1}$). Therefore, this minor variation in the spectral response allows a direct comparison between the NA and isotopically enriched hyperlenses at the same incident frequencies, while preserving roughly equal values for the real part of the permittivity. Additionally, the thicknesses of the two devices are identical, thereby isolating the role that loss reduction plays in improving hyperlens performance.

To compare the imaging performance of NA hBN and h¹¹BN, we first measured the hyperlens fields resulting from a 44 nm diameter disk embedded beneath each of the two hBN slabs, with the fields collected via s-SNOM (Figure 2a,b). The lower losses of h¹¹BN (Figure 2a) lead to a stronger s-SNOM amplitude in comparison to that observed with NA hBN at the same frequencies (Figure 2b). The improved signal amplitude also leads to more internal reflections (Figure 2a,c vs Figure 2b,d). To quantitatively compare the transmission efficiency between the two forms of hBN, we benchmark the peak signal to noise ratio (PSNR). While the noise levels for both s-SNOM images are comparable (section IV in the Supporting Information), the amplitude of the collected signal from the h¹¹BN hyperlens is much stronger. Specifically, line scans from

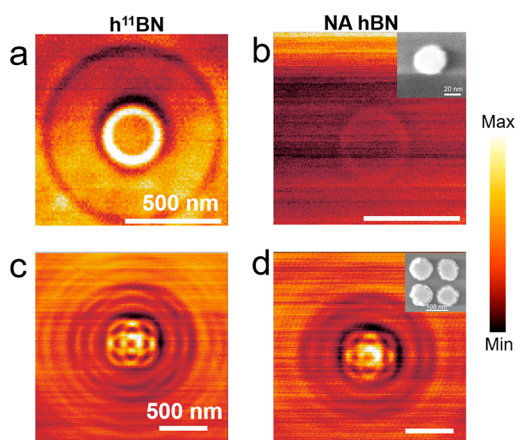


Figure 2. Experimental demonstration of superhigh-resolution subdiffractive focusing and imaging through natural and mono-isotopically enriched hBN. (a, b). Near-field amplitude image of a 44 nm square at $\omega = 1500 \text{ cm}^{-1}$ for ^{11}B and NA-hBN, respectively. (c, d) Near-field amplitude image of a 2×2 , 100 nm disk array with 25 nm gap separation at $\omega = 1480 \text{ cm}^{-1}$ for ^{11}B and NA-hBN, respectively. The corresponding SEM images are shown in the inserts of (b) and (d).

this hyperlens field (Figure S4a) indicate that the signal is far above the noise level, resulting in a PSNR of 11.5. In contrast, the comparable hyperlens fields using NA hBN are just resolvable due to low signal strength, with a corresponding PSNR of only 3.64 (Figures S3 and S4a and Table S1). Although the measured hyperlens fields are not direct magnified replicas of underlying objects, they can be reconstructed to resolve the image. Thus, those high-PSNR hyperlens fields of 44 nm disks indicate a subdiffractive imaging resolution following reconstruction of at least $\lambda_{\text{FS}}/154$ ($\omega = 1480 \text{ cm}^{-1}$, $\lambda_{\text{FS}} = 6.76 \mu\text{m}$) for both hyperlens systems, a nearly 4-fold improvement over previous reports with NA hBN.^{5,8} Additionally, on the basis of the comparative PSNR

values, $\lambda_{\text{FS}}/154$ does not represent the imaging power limit of the mono-isotopic hyperlens but instead represents simply the smallest structures realized in this study, as the empirical resolution is determined by signal strength (section IX in the Supporting Information). Thus, it is anticipated that the $h^{11}\text{BN}$ hyperlens can provide substantial additional resolving power for even smaller objects, while the NA device is at or close to its resolving power. This overall improvement via $h^{11}\text{BN}$ thereby facilitates the transition to thicker and/or curved films for far-field hyperlens approaches.

For practical use, a hyperlens must resolve not only isolated objects but also multiple closely spaced structures. To validate this capability, we consider a 2×2 array of 100 nm diameter, 30 nm tall nickel disks with nominal separation distances of 25 nm (a top-view SEM image is shown in the inset of Figure 2d). The corresponding hyperlens fields were collected via s-SNOM for both the $h^{11}\text{BN}$ and NA-hBN flakes with an incident laser at $\omega = 1480 \text{ cm}^{-1}$, as provided in Figure 2c,d, respectively. Consistent with the imaging of single disks, the image quality is superior for those collected through the $h^{11}\text{BN}$ slab, as visualized in Figure 2c,d. Quantitatively, the $h^{11}\text{BN}$ hyperlens leads to a higher PSNR (37.75) in comparison to the NA slab (11.32) (see Figure S4b and Table S1).

While these efforts highlight improvements in the PSNR for the collected hyperlens fields, directly identifying the underlying objects from these measurements is still challenging. Because HPhP rays are launched from all edges of the object in all directions, the resultant concentric patterns give rise to complicated fields even for simple systems such as an isolated disk (Figure 2a). For more complex objects or multiple closely spaced structures, such patterns highlight extensive interference between the overlapping HPhP rays, complicating the collected fields (Figure 2c). In other words, the observed hyperlens fields are not direct expansions of underlying objects, which must be reconstructed for practical applications.

To address this challenge, we use the angular spectrum method to back-propagate the measured fields at the hBN slab

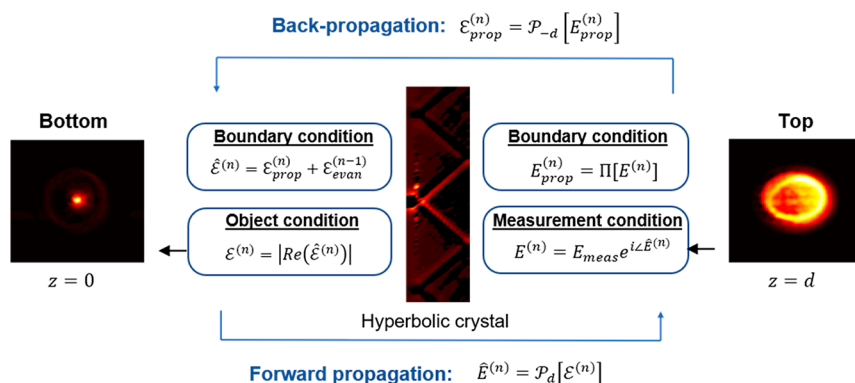


Figure 3. Algorithm flowchart. The algorithm iterates between the experimentally measured field amplitude at the top of the crystal and the object field at the bottom of the crystal. The rightmost image shows a sample measurement of the crystal output, the central image depicts approximate ray paths within the crystal, and the leftmost image represents the input field reconstruction after 200 iterations. We start the algorithm by enforcing the measurement conditions; E_{meas} is the measured field, \angle denotes the phase of the complex field (to be found), and n represents the iteration number. The projection operator Π extracts the propagating modes from $E^{(n)}$ by enforcing the boundary constraints on the input and output faces of the crystal. The angular-spectrum propagation operator \mathcal{P}_d transports the propagating modes of the input field by a distance d . To match the boundary conditions at the bottom of the crystal, we add the evanescent modes (obtained from the previous iteration $\hat{E}^{(n-1)}$) to get the total field $\hat{E}^{(n)}$. We further apply the small object constraint to get our reconstruction. The subscripts prop and evan represent propagating and evanescent components of a given electric field, respectively, $\text{Re}(\cdot)$ represents the real part of (\cdot) , and $|\cdot|$ represents an absolute value operation. $\hat{\cdot}$ denotes the estimated quantity of (\cdot) .

surface to the unknown scattering source at the bottom surface. Although a single-step back-propagation is sufficient to determine the bottom field (underlying patterns) with fields measured by our *s*-SNOM (section V in the Supporting Information), where the amplitude and phase are both provided, it is not trivial to acquire the phase in far-field hyperlens concepts, and it might not be practical to get the phase in some measurement setups: e.g., photothermal infrared (PTIR). Thus, to provide a generalized solution, we developed an iterative back-propagation algorithm to retrieve the fields under hyperbolic media with only amplitude information. The algorithm is a modified Gerchberg–Saxton (GS) algorithm,²⁴ as illustrated in the flowchart provided in Figure 3. In the case of *s*-SNOM, only the *z* component of the *E* field, E_z , is measured by the *s*-SNOM tip. Nevertheless, propagation in the hBN is anisotropic; therefore, the full vector near field of the object must be retrieved. The algorithm starts with the measured *s*-SNOM image as the top-field profile, and the measured field is back-propagated to the bottom side of hBN by the inverse propagation function P_{-i} . From there, the field of the bottom object, representing the position and size of the object under hBN, can be extracted. The bottom field is then forward-propagated to the top surface and then back-propagated again to the bottom, and the difference between the “calculated top field” and “measured top field” is decreased during such an iteration. Iterations are continued until the calculated top field converges (within a predetermined error) to the measured field distribution from *s*-SNOM. To match the boundary conditions at the bottom surface, this reconstruction includes evanescent and propagating modes. Empirically, we found that the incident field could be approximated with linearly independent plane waves (valid since the object is much smaller than the wavelength of light), while the field inside the crystal could be modeled as a joint (scalar) field hybridizing the two polarizations. Forward-propagation consists of the following steps: (1) coupling the light from the illumination source into the crystal, (2) advancing the propagating modes to the top surface (an approximation that gets better with increasing slab thickness), and (3) replacing the joint field with the experimentally measured field. In our algorithm, we ignored the internal reflections, as they did not provide any new information to the algorithm. However, we believe that they will become crucial if we want to relax the small-object constraint or are working in a low signal to noise regime. More details of the algorithm are given in section VI in the Supporting Information. Note that the reconstructed patterns are actually the electrical field under the hyperbolic materials, which are the positions and sizes of disks in our system. However, the fields under hyperbolic materials are not necessarily equal to the underlying patterns when the fields are altered by coupling/resonant behaviors.

To test the reconstruction algorithm, hyperlens fields were collected from the $h^{11}\text{BN}$ hyperlens over the 2×2 , 100 nm diameter dot array with a 25 nm gap at various frequencies (Figure 4a–d). The acquired hyperlens fields are significantly different at each frequency and illustrate consistency with predicted fields via finite element method (FEM) simulations, as shown in Figure 4e–h. Note that additional speckling is observed in FEM simulations, caused by multiple high-order HPhPs superimposed upon each other. To minimize the speckling so that the simulated hyperlens fields are easier to interpret, the simulations in Figure 4 are performed with a 3-

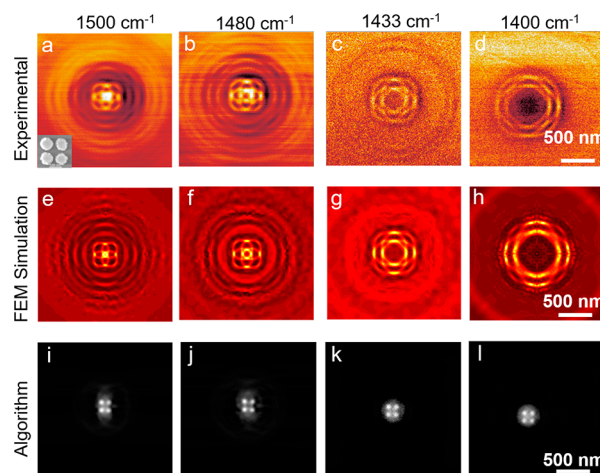


Figure 4. Frequency-dependent hyperlens fields and reconstruction. (a–d) Near-field amplitude images of an ~ 100 nm disk array with 25 nm interparticle gaps, showing a strong dependence on the HPhP propagation angle. (e–h) Corresponding FEM simulations. (i–l) Reconstructed underlying structures from the corresponding *s*-SNOM images.

fold artificially increased loss of $h^{11}\text{BN}$, and FEM simulations using the correct loss are included in Figure S9.

Despite the complexity in the hyperlens fields from the 2×2 disk arrays (Figure 4), the reconstruction algorithm successfully retrieves underlying structures featuring the accurate size and alignment, as shown in Figure 4i–l. The extracted diameter and interparticle gaps of the disks, averaged over the four incident frequencies, are 87 and 27 nm, respectively, which agree with the actual diameter (~ 100 nm) and gap values (~ 25 nm). Notably, the image reconstructions were performed at multiple frequencies, i.e., different hyperbolic angles (eq 1), all showing excellent agreement with the actual size measured by SEM (Table S3). Such an ability is of significant importance for resonant materials, e.g., biomaterials, since imaging on/off resonance could provide strong material contrast,^{25,26} potentially useful in material identification. Additionally, those multifrequency measurements can be correlated to refine the retrieved image, known as label fusion in the machine-learning field. Beyond imaging applications, this algorithm can extract the material thickness or fine-tune the material dielectric properties,²⁷ such as the recent use of near-field measurements for optimizing the dielectric function of the biaxial hyperbolic crystal MoO_3 .²⁸

With those efforts, we have validated the superiority of monoisotopic-hBN-enabled hyperlens in the near field. As the far-field hyperlens is the eventual goal, we extend our discussion to predict the performance of an hBN-based far-field hyperlens. For far-field hyperlens designs, the empirical resolution is dictated by loss.¹¹ Higher resolution requires thicker hyperbolic materials, yet thicker hyperbolic media increase the loss and reduce the signal, with the lowest acceptable signal being the noise equivalent power. In other words, a lower loss allows thicker hyperbolic media to be used, and therefore, higher resolution hyperlens fields to be measured. Thus, we evaluate the loss of hyperbolic materials to provide insights into optimizing near- or far-field hyperlens measurements. To describe the attenuation of the HPhPs propagating through the hBN slab, the quality factor (Q) is defined as^{29,30}

$$Q = \frac{k'}{k''} = 4\pi N \quad (2)$$

where k' and k'' are the real and imaginary parts of the wavevector, respectively, and N defines the number of cycles before the HPhP wave decays to $1/e$. Thus, increasing Q implies a stronger hyperlens signal, and hence a higher spatial resolution. To find k'' , an analytical model^{3,29–31} is employed to calculate both the real and imaginary part of the HPhP wavevectors propagating in hBN over any material:

$$k(w) = k' + ik'' = -\frac{\psi}{t} \left[a \tan\left(\frac{\epsilon_o}{\epsilon_t \psi}\right) + a \tan\left(\frac{\epsilon_s}{\epsilon_t \psi}\right) + \pi l \right]$$

$$\psi = -i \sqrt{\frac{\epsilon_z}{\epsilon_t}} \quad (3)$$

where t represents the hBN thickness and ϵ_o and ϵ_s represent the complex dielectric functions of air and the substrate, respectively, while l represents the HPhP mode order (here $l = 1$ is the primary mode of interest). Using this analytical model, we plot the Q factor of $h^{11}\text{BN}$ as a function of the incident (imaging) frequency in Figure 5, and we find that the Q factor

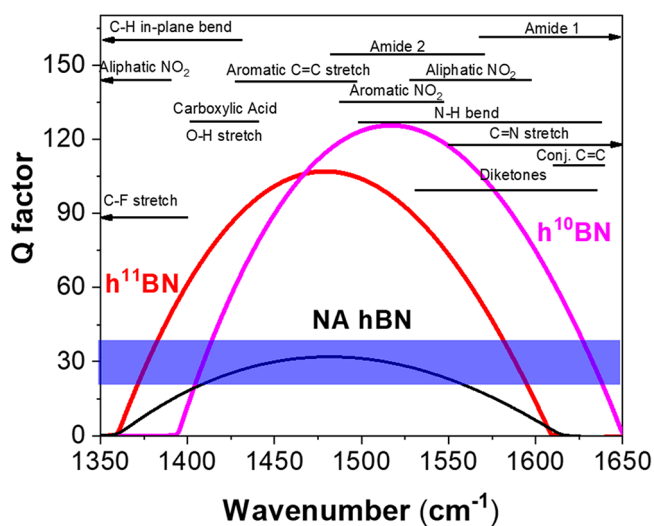


Figure 5. The Q factor for hyperlens imaging with different materials. The Q factor for hyperlens imaging as defined in the main text is presented for NA-hBN (black curve) along with both $h^{11}\text{BN}$ (red curve) and $h^{10}\text{BN}$ (magenta curve) materials. The spectral range associated with a number of different chemical vibrational modes of interest are also provided, each designated by the extents of the black lines, with arrows indicating the spectral range extends beyond that of the reststrahlen band. The blue transparent ribbon is the artificial HMM made of sodium and silicon.

is highest at around 1490 cm^{-1} for both NA and $h^{11}\text{BN}$. As the hyperlens performance is related to loss, we anticipate that the best image quality occurs at $\sim 1490\text{ cm}^{-1}$, which agrees with our experimental observations (Figure 4). Although the analytical solution is not quantitatively accurate when the HPhP wavevectors are not significantly larger than the free-space values (more discussions are given in section VIII in the Supporting Information), this approach still provides qualitative guidance toward optimizing hyperlens operation and design in this regime as well.

While the frequency is critical in the performance of a hyperlens, we stress that the material advantage is vital. By

comparing the Q factors of $h^{11}\text{BN}$ and NA hBN, we estimate that $h^{11}\text{BN}$ provides an approximately 3-fold increase in transmission, causing better image quality over the entire upper Reststrahlen band (URB), as shown in Figure 5. Consistent with the calculation, the PSNR of hyperlens fields collected using $h^{11}\text{BN}$ are indeed 3 times larger than those using NA hBN, as discussed earlier and presented in Figure 2, Figure S4, and Table S1. We also compare the performance of hBN with artificial HMM composed of ultralow-loss sodium plasma material³² (blue ribbon in Figure 5), again showing the superiority of monoisotopic hBN for hyperlensing applications (details of calculations are given in section VIII in the Supporting Information). Notably, the Q factor of an artificial HMM made of silver is ~ 10 in the MIR, which is a factor of 3 worse than even NA hBN.

It is important to note that spectral overlaps between the URB of hBN and the MIR molecular fingerprint region enable the potential for resonant hyperlens imaging (Figure 5). For resonant imaging of biomaterials, the measured field will be altered by the chemical vibrational frequencies;^{25,26} thus, imaging at different frequencies will provide both spatial information and chemical identifications. As $h^{11}\text{BN}$ and $h^{10}\text{BN}$ together cover a broad range of vibrational frequencies of interest, e.g., the amide I and II bands of proteins³³ (overlaid black lines in Figure 5), hBN-enabled hyperlens can be applied on those biomaterials. Therefore, for different purposes, these two monoisotopic hBN materials (and potentially $h^{10}\text{B}^{15}\text{N}$ and $h^{11}\text{B}^{15}\text{N}$ if grown, as recently demonstrated for cBN) could be used to optimize such imaging methodologies even further.

CONCLUSION

In conclusion, through the exploitation of ultralow-loss $h^{11}\text{BN}$ hyperlens devices, we demonstrate the ability to resolve the smallest features we fabricated ($\sim 44\text{ nm}$), showing a record-high imaging resolution of at least $\lambda_{\text{FS}}/154$, which is a nearly 4-fold improvement over previously reported data using NA hBN material.^{5,8} Additionally, we demonstrate the ability to discern four closely spaced $\sim 100\text{ nm}$ disks, even at interparticle separations of 25 nm , indicating the potential for imaging objects with separations that are on the order of $\lambda_{\text{FS}}/270$. Note that the high PSNR of $h^{11}\text{BN}$ hyperlens fields suggests that the ultimate resolution limit has yet to be reached. Furthermore, the transmission of $h^{11}\text{BN}$ is predicted to be 3 times higher than that of NA hBN, which is consistent with the experimentally measured 3-fold increment of PSNR, providing significant opportunities in employing thicker and/or curved hyperbolic media for far-field hyperlens. Further, using a numerical algorithm, we demonstrate precise image reconstruction and accurately retrieve the details of the embedded 2×2 , $\sim 100\text{ nm}$ disk array with $\sim 25\text{ nm}$ gaps, validating this as a potential methodology for detecting unknown subdiffractional objects. Combining the numerical algorithm and ultralow-loss monoisotopic hBN, we provide a broad potential of imaging modalities, such as resonant hyperlens imaging with incident frequencies coincident with the vibrational frequencies of materials. We also offer analytical calculations of the frequency dependence of Q , necessary for realizing optimal performance. Therefore, this work also more broadly serves as a roadmap for designing hyperlenses using other newly discovered hyperbolic materials^{17,28,34–44} for subdiffractional imaging, focusing, and label-free detection.

METHODS

Subdiffractive Object Fabrication. To realize the hyperlens concept, subdiffractive nickel (Ni) disks were patterned on SiO₂ substrates using a Raith-150 electron beam writer. For the fabrication of the fine features by e-beam lithography, we used the ZEP520 resist. The e-write was followed by resist development, metal deposition, and lift-off to realize the 30 nm thick Ni structures.

Device Fabrication. We used two forms of hBN crystals in our study, the naturally abundant and ¹¹B-enriched forms. The NA was procured from HQ Graphene, while the monoisotopic hBN crystals were grown by the precipitation of hBN synthesized from nitrogen and elemental ¹¹B (99.4%) from a molten metal flux of nickel and chromium. The crystal growth techniques utilized for h¹¹BN are described in refs 20 and 45. Both types of hBN flakes of various thicknesses were obtained by standard exfoliation from the bulk crystals onto a PMMA/PVA (poly(vinyl acetate)) bilayer stack on a silicon wafer. The PMMA/hBN stack was carefully and precisely transferred onto the fabricated hyperlens pattern, finally washing off the PMMA to obtain the hBN-based hyperlens devices. More details of this transfer technique are given in ref 46.

Near-Field Imaging (Infrared s-SNOM Measurements and Analysis). Infrared nanoimaging was performed with a commercial (Neaspec GmbH) scattering-type scanning near-field optical microscope (s-SNOM) based on a tapping-mode atomic force microscope. A quantum cascade laser (DRS Daylight Solutions) was used as the light source, which was focused onto a metallic tip oscillating at a tapping frequency of ~250 kHz with a tapping amplitude of around 60 nm. The scattered light was detected using a liquid-nitrogen-cooled HgCdTe (MCT) detector. To suppress far-field background signals, the detected signal was demodulated at the harmonic *n* of the tapping frequency. In this work, we used *n* = 3. An additional description of the s-SNOM technique is available elsewhere.⁴⁷ The data presented in the paper were collected from two systems: system 1 at Columbia University and system 2 at Vanderbilt University.

Numerical Simulation of Near Fields and Spectra. Electromagnetic simulations of hyperlens fields on the top of hBN were carried out using the frequency-domain solver in CST Studio Suite 2018. The model consisted of a 125 nm thick slab of hBN (lateral size 5 μm) on top of Ni disks matching the experiment, which were placed onto a 270 nm thick thermal SiO₂ substrate. This model was excited through the substrate with normal incidence plane waves using Floquet boundary conditions. In order to minimize speckling in the simulated fields, the nickel disk edges were rounded (blend radius 10 nm), and the mesh density was enhanced to a maximum tetrahedral dimension of 3 nm within the nickel disks themselves. Furthermore, the mesh density was also enhanced to 30 nm within the hBN in a 1 μm square above the disks. Further, for the simulations in Figure 4, the damping constant of h¹¹BN was increased 3-fold. We rotated the extracted field of one polarization and summed it with the unrotated one to reproduce the experimentally measured image.

ASSOCIATED CONTENT

Supporting Information

The Supporting Information is available free of charge at <https://pubs.acs.org/doi/10.1021/acs.nanolett.1c01808>.

s-SNOM of disk array within and outside the reststrahlen band, AFM topography and s-SNOM images for an isolated 40 nm disk and a 2 × 2 disk array under the isotopically enriched material, s-SNOM images acquired by different systems, signal to noise ratio characterization, Frequency-dependent s-SNOM amplitude and phase comparisons, image reconstruction algorithm, influence of low losses of h¹¹BN on simulated hyperlens fields, accuracy of the analytical solution, and the resolution, empirically limited by loss (PDF)

AUTHOR INFORMATION

Corresponding Author

Joshua D. Caldwell – Department of Mechanical Engineering, Vanderbilt University, Nashville, Tennessee 37212, United States; orcid.org/0000-0003-0374-2168; Email: josh.caldwell@vanderbilt.edu

Authors

Mingze He – Department of Mechanical Engineering, Vanderbilt University, Nashville, Tennessee 37212, United States; orcid.org/0000-0001-8773-1268

Ganjigunte R. S. Iyer – ASEE/NRC Postdoctoral Fellow residing at NRL, Washington, D.C. 20375, United States; U.S. Naval Research Laboratory, Washington, D.C. 20375, United States

Shaurya Aarav – Department of Electrical Engineering, Princeton University, Princeton, New Jersey 08544, United States

Sai S. Sunku – Department of Physics, Columbia University, New York, New York 10027, United States; orcid.org/0000-0002-7037-8717

Alexander J. Giles – U.S. Naval Research Laboratory, Washington, D.C. 20375, United States

Thomas G. Folland – Department of Mechanical Engineering, Vanderbilt University, Nashville, Tennessee 37212, United States; Department of Physics and Astronomy, The University of Iowa, Iowa City, Iowa 52242, United States

Nicholas Sharac – ASEE/NRC Postdoctoral Fellow residing at NRL, Washington, D.C. 20375, United States

Xiaohang Sun – Department of Electrical Engineering, Princeton University, Princeton, New Jersey 08544, United States

Joseph Matson – Department of Mechanical Engineering, Vanderbilt University, Nashville, Tennessee 37212, United States

Song Liu – Tim Taylor Department of Chemical Engineering, Kansas State University, Manhattan, Kansas 66506, United States; orcid.org/0000-0002-3046-3335

James H. Edgar – Tim Taylor Department of Chemical Engineering, Kansas State University, Manhattan, Kansas 66506, United States

Jason W. Fleischer – Department of Electrical Engineering, Princeton University, Princeton, New Jersey 08544, United States

D. N. Basov – Department of Physics, Columbia University, New York, New York 10027, United States

Complete contact information is available at: <https://pubs.acs.org/doi/10.1021/acs.nanolett.1c01808>

Author Contributions

[○]M.H., G.R.S.I., and S.A. contributed equally to the paper.

Notes

The authors declare no competing financial interest.

ACKNOWLEDGMENTS

Research on hBN nanostructures at Columbia was supported by the Vannevar Bush Faculty Fellowship ONR-VB: N00014-19-1-2630, and NSF/EFRI-1741660. The development of nanoimaging capabilities at Columbia was supported as part of Programmable Quantum Materials, an Energy Frontier Research Center funded by the U.S. Department of Energy (DOE), Office of Science, Basic Energy Sciences (BES), under award DE-SC0019443. D.N.B. is a Moore Investigator in Quantum Materials EPIQS #9455. HL device fabrication at NRL was supported by an ASEE fellowship, with funding for NRL work provided by the Office of Naval Research through the Nanoscience Institute. Computational imaging at Princeton was supported by the Air Force Office of Scientific Research (AFOSR) under Grant FA9550-18-1-029. Support for hBN crystal growth from the Office of Naval Research by award N00014-20-1-2427 is appreciated. Imaging work at Vanderbilt was supported for M.H. and J.D.C. by ONR-N00014-18-1-2107, while J.M. was supported by the National Science Foundation, Division of Materials Research, under grant number 1904793. The data that support the findings of this study are available from the corresponding author on reasonable request.

REFERENCES

- (1) Poddubny, A.; Iorsh, I.; Belov, P.; et al. Hyperbolic metamaterials. *Nat. Photonics* **2013**, *7*, 948.
- (2) Caldwell, J. D.; Kretinin, A. V.; Chen, Y.; et al. Sub-diffractive volume-confined polaritons in the natural hyperbolic material hexagonal boron nitride. *Nat. Commun.* **2014**, *5*, 5221.
- (3) Dai, S.; Fei, Z.; Ma, Q.; et al. Tunable phonon polaritons in atomically thin van der Waals crystals of boron nitride. *Science* **2014**, *343*, 1125–1129.
- (4) Ishii, S.; Kildishev, A. V.; Narimanov, E.; et al. Sub-wavelength interference pattern from volume plasmon polaritons in a hyperbolic medium. *Laser & Photonics Reviews* **2013**, *7*, 265–271.
- (5) Li, P.; Lewin, M.; Kretinin, A. V.; et al. Hyperbolic phonon-polaritons in boron nitride for near-field optical imaging and focusing. *Nat. Commun.* **2015**, *6*, 7507.
- (6) Wang, W.; et al. Far-field imaging device: planar hyperlens with magnification using multi-layer metamaterial. *Opt. Express* **2008**, *16* (25), 21142–21148.
- (7) Sun, J.; Litchinitser, N. M. Toward practical, subwavelength, visible-light photolithography with hyperlens. *ACS Nano* **2018**, *12* (1), 542–548.
- (8) Dai, S.; Ma, Q.; Andersen, T.; et al. Subdiffractive focusing and guiding of polaritonic rays in a natural hyperbolic material. *Nat. Commun.* **2015**, *6*, 6963.
- (9) Liu, Z.; Lee, H.; Xiong, Y.; et al. Far-field optical hyperlens magnifying sub-diffraction-limited objects. *Science* **2007**, *315*, 1686–1686.
- (10) Rho, J.; Ye, Z.; Xiong, Y.; et al. Spherical hyperlens for two-dimensional sub-diffractive imaging at visible frequencies. *Nat. Commun.* **2010**, *1*, 1–5.
- (11) Lee, D.; Kim, Y. D.; Kim, M.; et al. Realization of wafer-scale hyperlens device for sub-diffractive biomolecular imaging. *ACS Photonics* **2018**, *5*, 2549–2554.
- (12) Xiong, Y.; Liu, Z.; Zhang, X. A simple design of flat hyperlens for lithography and imaging with half-pitch resolution down to 20 nm. *Appl. Phys. Lett.* **2009**, *94*, 203108.
- (13) Lu, D.; Liu, Z. Hyperlenses and metalenses for far-field super-resolution imaging. *Nat. Commun.* **2012**, *3*, 1205.
- (14) Ma, C.; Liu, Z. A super resolution metalens with phase compensation mechanism. *Appl. Phys. Lett.* **2010**, *96*, 183103.
- (15) Zheng, Z.; Jiang, J.; Xu, N.; et al. Controlling and focusing of in-plane hyperbolic phonon polaritons in α -MoO₃ with plasmonic antenna. 2021, arXiv:2103.17016v1. ArXiv preprint. <https://arxiv.org/abs/2103.17016v1> (March 31, 2021).
- (16) Dai, S.; Tymchenko, M.; Xu, Z.-Q.; et al. Internal nanostructure diagnosis with hyperbolic phonon polaritons in hexagonal boron nitride. *Nano Lett.* **2018**, *18*, 5205–5210.
- (17) Sun, J.; Litchinitser, N. M.; Zhou, J. Indefinite by nature: from ultraviolet to terahertz. *ACS Photonics* **2014**, *1*, 293–303.
- (18) Caldwell, J. D.; Aharonovich, I.; Cassabois, G.; et al. Photonics with hexagonal boron nitride. *Nature Reviews Materials* **2019**, *4*, 552–567.
- (19) Hoffman, T. B.; Clubine, B.; Zhang, Y.; et al. Optimization of Ni–Cr flux growth for hexagonal boron nitride single crystals. *J. Cryst. Growth* **2014**, *393*, 114–118.
- (20) Liu, S.; He, R.; Xue, L.; et al. Single crystal growth of millimeter-sized monoisotopic hexagonal boron nitride. *Chem. Mater.* **2018**, *30*, 6222–6225.
- (21) Liu, S.; He, R.; Ye, Z.; et al. Large-scale growth of high-quality hexagonal boron nitride crystals at atmospheric pressure from an Fe–Cr flux. *Cryst. Growth Des.* **2017**, *17*, 4932–4935.
- (22) Giles, A. J.; Dai, S.; Vurgaftman, I.; et al. Ultralow-loss polaritons in isotopically pure boron nitride. *Nat. Mater.* **2018**, *17*, 134.
- (23) Cuscó, R.; Edgar, J. H.; Liu, S.; et al. Isotopic Disorder: The Prevailing Mechanism in Limiting the Phonon Lifetime in Hexagonal BN. *Phys. Rev. Lett.* **2020**, *124*, 167402.
- (24) Gerchberg, R. W. A practical algorithm for the determination of phase from image and diffraction plane pictures. *Optik* **1972**, *35*, 237–246.
- (25) Wang, C.-F.; Kafle, B.; Tesema, T. E. Molecular Sensitivity of Near-Field Vibrational Infrared Imaging. *J. Phys. Chem. C* **2020**, *124*, 21018–21026.
- (26) Bylinkin, A.; Schnell, M.; Autore, M.; et al. Real-space observation of vibrational strong coupling between propagating phonon polaritons and organic molecules. *Nat. Photonics* **2021**, *15*, 197–202.
- (27) Barsi, C.; Wan, W.; Fleischer, J. W. Imaging through nonlinear media using digital holography. *Nat. Photonics* **2009**, *3*, 211–215.
- (28) Álvarez-Pérez, G.; Folland, T. G.; Errea, I. Infrared Permittivity of the Bixial van der Waals Semiconductor α -MoO₃ from Near- and Far-Field Correlative Studies. *Adv. Mater.* **2020**, *32*, 1908176.
- (29) Fali, A.; White, S. T.; Folland, T. G.; et al. Refractive Index-Based Control of Hyperbolic Phonon-Polariton Propagation. *Nano Lett.* **2019**, *19*, 7725–7734.
- (30) Dai, S.; Quan, J.; Hu, G.; et al. Hyperbolic phonon polaritons in suspended hexagonal boron nitride. *Nano Lett.* **2019**, *19*, 1009–1014.
- (31) He, M.; Halimi, S. I.; Folland, T. G.; et al. Guided Mid-IR and Near-IR Light within a Hybrid Hyperbolic-Material/Silicon Waveguide Heterostructure. *Adv. Mater.* **2021**, *33*, 2004305.
- (32) Wang, Y.; Yu, J.; Mao, Y.-F.; et al. Stable, high-performance sodium-based plasmonic devices in the near infrared. *Nature* **2020**, *581*, 401–405.
- (33) Chatzakos, I.; Krishna, A.; Culbertson, J.; et al. Strong confinement of optical fields using localized surface phonon polaritons in cubic boron nitride. *Opt. Lett.* **2018**, *43*, 2177–2180.
- (34) Korzeb, K.; Gajc, M.; Pawlak, D. A Compendium of natural hyperbolic materials. *Opt. Express* **2015**, *23*, 25406–25424.
- (35) Low, T.; Chaves, A.; Caldwell, J. D.; et al. Polaritons in layered two-dimensional materials. *Nat. Mater.* **2017**, *16*, 182–194.
- (36) Ma, W.; Alonso-González, P.; Li, S.; et al. In-plane anisotropic and ultra-low-loss polaritons in a natural van der Waals crystal. *Nature* **2018**, *562*, 557.
- (37) Zheng, Z.; Chen, J.; Wang, Y.; et al. Highly confined and tunable hyperbolic phonon polaritons in van der Waals semiconducting transition metal oxides. *Adv. Mater.* **2018**, *30*, 1705318.

- (38) Taboada-Gutiérrez, J.; Álvarez-Pérez, G.; Duan, J.; et al. Broad spectral tuning of ultra-low-loss polaritons in a van der Waals crystal by intercalation. *Nat. Mater.* **2020**, *19*, 964.
- (39) Chen, M.; Lin, X.; Dinh, T. H.; et al. Configurable phonon polaritons in twisted α -MoO₃. *Nat. Mater.* **2020**, *19*, 1307–1311.
- (40) Duan, J.; Capote-Robayna, N.; Taboada-Gutiérrez, J.; et al. Twisted nano-optics: Manipulating light at the nanoscale with twisted phonon polaritonic slabs. *Nano Lett.* **2020**, *20*, 5323–5329.
- (41) Hu, G.; Ou, Q.; Si, G.; et al. Topological polaritons and photonic magic angles in twisted α -MoO₃ bilayers. *Nature* **2020**, *582*, 209–213.
- (42) Sun, F.; Huang, W.; Zheng, Z.; et al. Polariton waveguide modes in two-dimensional van der Waals crystals: an analytical model and correlative nano-imaging. *Nanoscale* **2021**, *13*, 4845–4854.
- (43) Zheng, Z.; Sun, F.; Huang, W.; et al. Phonon polaritons in twisted double-layers of hyperbolic van der Waals crystals. *Nano Lett.* **2020**, *20*, 5301–5308.
- (44) Basov, D. N.; Asenjo-Garcia, A.; Schuck, P. J.; et al. Polariton panorama. *Nanophotonics* **2020**, *10*, 549–577.
- (45) Vuong, T.; Liu, S.; Van der Lee, A.; et al. Isotope engineering of van der Waals interactions in hexagonal boron nitride. *Nat. Mater.* **2018**, *17*, 152.
- (46) Kretinin, A.; Cao, Y.; Tu, J.; et al. Electronic properties of graphene encapsulated with different two-dimensional atomic crystals. *Nano Lett.* **2014**, *14*, 3270–3276.
- (47) Chen, X.; Hu, D.; Mescall, R. Modern Scattering-Type Scanning Near-Field Optical Microscopy for Advanced Material Research. *Adv. Mater.* **2019**, *31*, 1804774.